UNIVERSITY OF CALIFORNIA

SANTA CRUZ

**DETECTION METHODS FOR DISCOVERING EVAPORATING
PRIMORDIAL BLACK HOLES IN MODERN GAMMA-RAY
TELESCOPES**

A thesis submitted in partial satisfaction of the
requirements for the degree of

MASTER OF SCIENCE

in

PHYSICS

by

Xavier D. Boluna

March 2023

The Thesis of Xavier D. Boluna
is approved:

_____

Professor Stefano Profumo, Chair

_____

Professor Tesla Jeltema

_____

Professor Wolfgang Altmannshofer

_____

Peter Biehl
Vice Provost and Dean of Graduate Studies

Table of Contents

List of Figures

vi

List of Tables

Abstract

Detection methods for discovering Evaporating Primordial Black Holes in

modern Gamma-ray Telescopes

by

Xavier D. Boluna

The potential of directly observing a primordial black hole (PBH) explosion carries immense implications for our understanding of the universe, from cosmology to particle physics. While the existence of PBHs as a candidate for dark matter has been theorized for decades, direct detection of an evaporating PBH would provide invaluable insights into yet-undiscovered high-energy particles and dark radiation. In this thesis, we review the role of PBH as a dark matter candidate, including formation mechanisms and an overview of the state of the field. We model the detection limits for PBH sources in the γ photon spectrum for a number of modern telescopes and discuss constraints due to velocity dispersion, multi-spectral characteristics and lightcurve evolution. We investigate also the possibility and effect of dark particle radiation arising from dark degrees of freedom in black hole evaporation, and the possibility of a multi-spectral afterglow from PBH evaporation products. Lastly, we apply these novel constraints to the *Fermi* mission catalogs and produce several candidates at a variety of different possible evaporation stages and distances.

I dedicate this thesis to Gua Ma, Gua Kong, Avi and Yaya.

Acknowledgments

I would like to thank my adviser, Dr. Stefano Profumo, whose perfect blend of raw enthusiasm and patient guidance brought the science alive and kept me motivated through it all. I would like to thank Dr. Nicola Omodei and Tom Langenstein for helping me realize a wonderful opportunity and influencing the trajectory of my career. I am very fortunate to have found such great mentors always willing to dispense quality advice.

I would like to thank my parents, who have always advocated for my personal and academic growth. I am deeply thankful for the lessons they've taught me, and for their willingness to always provide second opinions, email proofreads and nuggets of wisdom. I can never thank you enough.

I count among family my childhood best friends, who always know how to put me at ease, and Maeve, who always grounds me and keeps my sanity intact. Thank you to the physics community at UC Santa Cruz, from the extraordinarily compassionate faculty to the many friends who made this beach town a home.

Part I

Properties of evaporating

primordial black holes

Chapter 1

Introduction

1.1 Dark matter

Dark matter owes its beginning to the discrepancy between the observed mass and the gravitational dynamics of many astrophysical structures. Dark matter is so named because it does not interact with light, however its influence on gravitationally-bound systems is empirically observed [19]. There are an abundance of astronomical methodologies which provide evidence for the existence of dark matter, from gravitational lensing to the evolution of large-scale structure of the Universe.

We know, for example, that the Keplerian prediction for the galactic rotation speed in our Milky Way $v_c(r) \propto \sqrt{\frac{M(r)}{r}}$ based on visible mass $M(r)$ is incompatible with the observed rotation curves [44]. We now attribute that missing mass to an abundance of dark matter in our solar system, typical to many similar spiral galaxies. This discrepancy is illustrated in **Figure 1.1**.
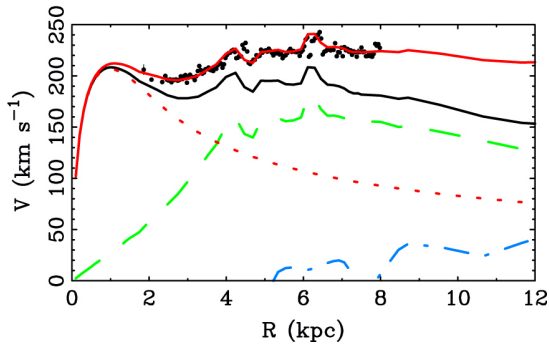
Figure 1.1: The Milky Way Galaxy's rotation speed. The difference between the Keplerian prediction $v_c \sim r^{-1/2}$ (red dotted line) and observed data (black dots) is quite significant. Additional spiral-arm components are also shown; stellar (green dashed) and gas disk (dot-dashed blue) and summed (red solid). Figure from reference [36].
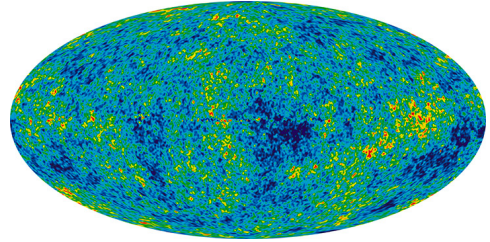
Figure 1.2: The Cosmic Microwave Background as observed by the Wilkinson Microwave Anisotropy Probe with galactic signal subtracted. Figure from reference [40].

Today, we estimate dark matter to contribute $\sim \frac{5}{6}$ of the universe's mass [53].Despite its apparent ubiquity, the exact nature and composition of dark matter is yet still a wide-open mystery in cosmology.

In the particle dark matter domain, there are rather broad available ranges for mass, interaction properties (so long as its photon radiation is sufficiently weak) and distribution. The two most widely studied are axions and weakly-interacting massive particles (WIMPs). The former are a very light ($< m_{e^-}$) class of primordial particles which dually solve CP-symmetry for strong interactions and interact weakly with ordinary matter. On the other hand, WIMPs would be long-lived and massive thermal relics from the early Universe, which only interact with the weak nuclear force [41]. This recipe happens also to be fulfilled by black holes, provided they are sufficiently light and of primordial origin.

3

1.2 Early universe perturbations

The Cosmic Microwave Background (CMB), pictured in **Figure 1.2**, is the remnant radiation of the early Universe from ~ 13.77 billion years ago. One of the important features of the CMB is that it is not perfectly uniform. It has tiny temperature variations known as anisotropies, and they are thought to be caused by fluctuations in the density of matter in the early universe [8].

Inflation theory describes the earliest moments following the Big Bang, a period of rapid expansion where these primordial mass density fluctuations could have been vastly amplified. Quantum field theory describes the creation and annihilation of virtual particles and antiparticles at near instantaneous timescales. In the current epoch, these fluctuations average to zero at large scale. During the inflation epoch, accelerated expansion stretched these quantum vaccuum fluctuations at the same rate as the Universe, and they evolved into classical perturbations [8]. Sufficiently large overdensities could then collapse to form black holes of a wide range of masses [13].

This method of black hole formation is in stark contrast with the only known creation mechanism for black holes in today's Universe: implosion of stars. Lacking stellar fusion products, stars contract under their own gravity until they are stabilized by fermion degeneracy pressure. Sufficiently massive stars beyond the Chandrasekhar limit $\gtrsim 10^{33}$g overcome degeneracy from electrons and neutrons, in turn, to collapse to form black holes [26]. Black holes do evaporate, though masses at this scale outlive the age of the Universe by several orders of magnitude. As such, we know that any black

holes lighter than stellar mass are impossible to create today and could only have been born in the early Universe. We refer to these black holes by their suspected origin: primordial black holes (PBHs).

1.3   Primordial black holes as dark matter

PBHs have long been suspected as possible culprits for dark matter, though their exact mass distribution and abundance is a matter of open debate. We can define today's fractional mass distribution as a function of total dark matter $f_{\mathrm{PBH}}(M_{\mathrm{PBH}}) = \rho_{\mathrm{PBH}}/\rho_{\mathrm{DM}}$ as a direct evolution of the primordial fractional mass distribution seeded by the CMB [16]. This evolution is sensitive to anything from mergers to WIMP halos, which could vary the size and density the resulting black holes. Shedding light on the modern mass function for primordial black holes is therefore invaluable for disentangling the history of large- and small-scale structure in the universe.

The current PBH mass distribution is constrained at the lower-end by the complete evaporation of black holes. Complete evaporation occurs only for black holes with a remaining lifetime less than the age of the Universe, corresponding to a mass $M(t_{\mathrm{Univ.}}) \simeq 5 \times 10^{14}\mathrm{g}$. Masses $M_{\mathrm{PBH}} < M(t_{\mathrm{Univ.}})$ have already expired and are can only be counted in their contribution to the extragalactic and galactic γ-ray background [27].

The extragalactic γ-ray background is essentially an integral of the contributions of all known γ-ray sources. Recent constraints in this domain have placed
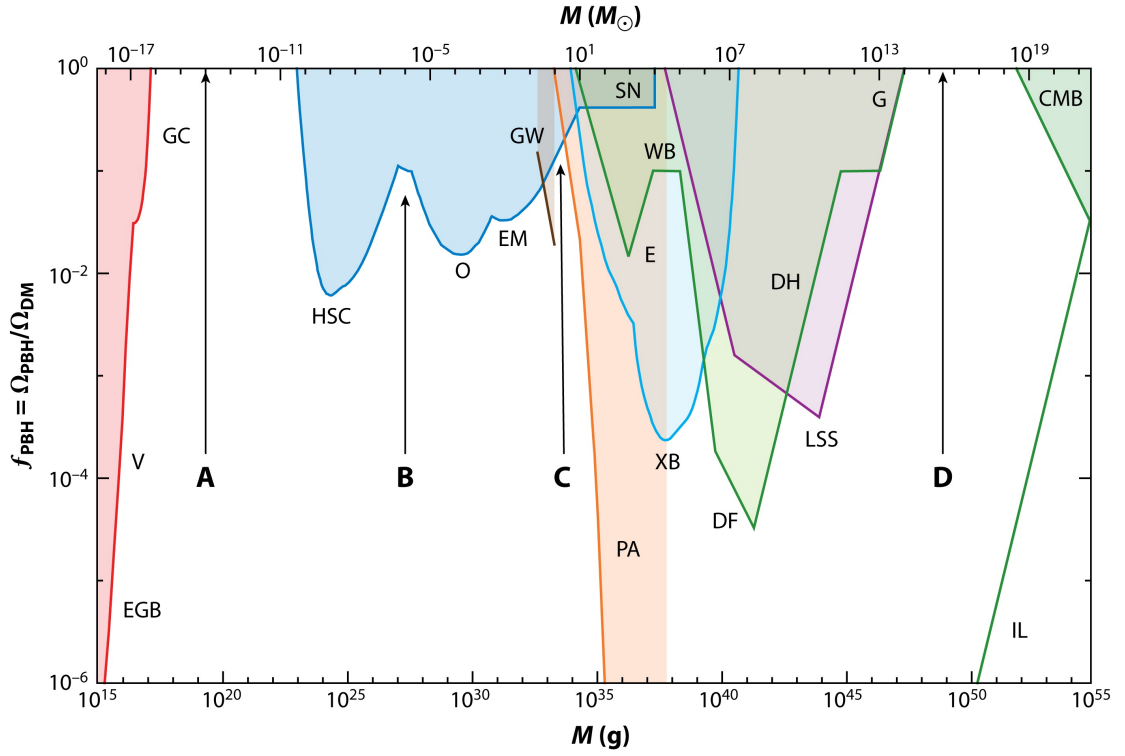
Figure 1.3: The modern state of constraints on f_{PBH}. The red shaded area constrains evaporation, including extragalactic γ-ray background (EGB) and galactic center anisotropy (GC) as discussed. Lensing constraints, shaded blue, provide the upper limit well-beyond evaporation masses. One of four open windows, asteroid-mass black holes (A) could exist near evaporation scales. Other constraints are derived from gravitational waves (GW), background distortions (orange), accretion (light blue), dynamical effects (green) and large-scale structure (purple). Figure from reference [15].

$f_{\mathrm{PBH}} \sim 10^{-7}$ [14]. In contrast, if there exists an abundance of black holes which are evaporating in increasing abundance right now, we expect to observe anisotropy in the γ-ray sky about the galactic center.

Surpassing masses close to $M(t_{\mathrm{Univ.}})$, non-evaporating black holes (named so, as they simply do not emit enough photons to be noticed observationally) are constrained by a variety of methods from gravitational lensing of distant stars to analysis of dynamical systems. Recent developments in gravitational wave astronomy could also detect (or constrain) nearby PBHs in evaporation mass scales [14]. Altogether, the available abundance of masses in which today's evaporating PBHs could lie is quite narrow. As we will discuss next, the potential in discovering PBHs born near $M(t_{\mathrm{Univ.}})$ is especially valuable – not only to understanding the evolution of the Universe, but also to our understanding of particle physics.

1.4   Black hole evaporation

The late Stephen Hawking described the ability for black holes to evaporate into subatomic particles by the same mechanism which produces PBHs in the first place. Vacuum fluctuations at the event horizon occasionally produce a particle pair for which one is absorbed by the black hole and the other escapes as Hawking radiation. In this way, any particles which escape must have rest mass less than or equal to the black hole temperature [26].

$$T_{\mathrm{PBH}} = \frac{\hbar c^3}{8\pi k_{\mathrm{B}} G M_{\mathrm{PBH}}} \approx 1.06 \left(\frac{10^{13} g}{M_{\mathrm{PBH}}} \right) \mathrm{GeV} \tag{1.1}$$

The evolution of the black hole's mass can therefore be described with respect to the function describing the allowed particle degrees of freedom, $\alpha(M_\mathrm{PBH})$ [25].

$$\frac{dM_\mathrm{PBH}}{dt} = -5.34 \times 10^{25} \left(\frac{\alpha(M_\mathrm{PBH})}{M_\mathrm{PBH}^2} \right) \mathrm{g\ s^{-1}} \tag{1.2}$$

In this way, a black hole's evaporation rate increases exponentially with time – culminating in an explosion at the end of its life. Black holes of any mass are subject to this evaporation and are therefore gifted a finite and deterministic lifetime [26]. Integrating the above equation and reparameterizing with respect to the PBH lifetime τ (see **section 2.1**) [25],

$$\tau \approx 6.24 \times 10^{-27} \left(\frac{M_\mathrm{PBH}^3}{\alpha(M_\mathrm{PBH})} \right) \mathrm{s} \tag{1.3}$$

PBHs which originated in the early universe $T_0 \sim 13.7$ Gyr would have masses 5×10^{14} g and would evaporate at present time [15]. Any smaller, and they will have already evaporated and would be "visible" only in their contribution to the γ-ray background [14].

1.5 Photon emission evolution

At masses $\gg 10^{17}$g PBHs only radiate photons and neutrinos ($\alpha \sim 1$). As such, the photon spectrum follows only the "direct" emission, dominated by photons of $E_\gamma \propto T_\mathrm{BH}$. As the evolution of a PBH continues, degrees of freedom become available which allow for quark and gluon jets to be emitted directly ($\alpha \sim 1.5$). These jets fragment into the particles and antiparticles of protons, electrons, neutrinos and photons. In the photon spectrum, this second "fragmentary" spectrum dominates at lower energies [35].

Figure 1.4 shows the photon spectra for several black hole temperatures, decomposed into the direct and fragmentary components. At low temperatures (30 MeV $\sim 10^{14}$g), photon radiation is largely dominated by the direct spectrum. As temperature increases, the direct spectrum continues evolving "forward" and fragmentary radiation sets the pace exceeding 300 MeV, creating the picture of a powerlaw progression for energy-integrated photon flux (**section 2.1**).

The domination of fragmentary radiation is crucial to this story and requires modelling of various collision and production models. These are informed by collider experiments near QCD confinement, for which the parameters are constantly being updated [47]. As such, fragmentary spectrum as it is modelled is sensitive to somewhat arbitrary choices of quark masses and the scale parameter Λ_{QCD} [14]. In general, we look to models of QCD when $T_{\mathrm{BH}} \gtrsim 200$ MeV [35].

In the late stages of PBH evaporation, $\alpha(M_{\mathrm{PBH}})$ would iterate over energies inaccessible to human collider projects. Supposing that there exist particles yet unknown to the Standard Model, observing of the spectral evolution of an "exploding" (as Hawking put it) black hole could reshape our understanding of material reality practically overnight. We attempt to parameterize some of this uncertainty in **section 2.8**, where we discuss the possible impact of dark particles radiation at high degrees of freedom on the energy-integrated flux lightcurve.
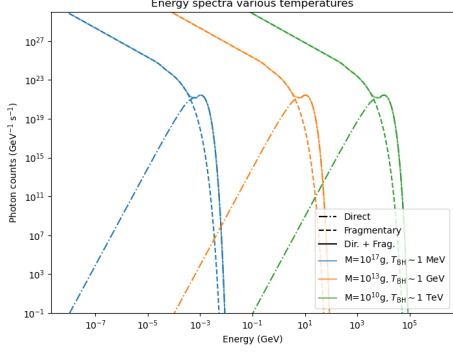
Figure 1.4: The photon spectrum evolution of a PBH as modelled at various temperatures using the parameterization given in Ukwatta, et. al. [51]. Solid lines represent total (summed) photon flux at the given temperature, while the composite lines indicate the direct and fragmentary emission.
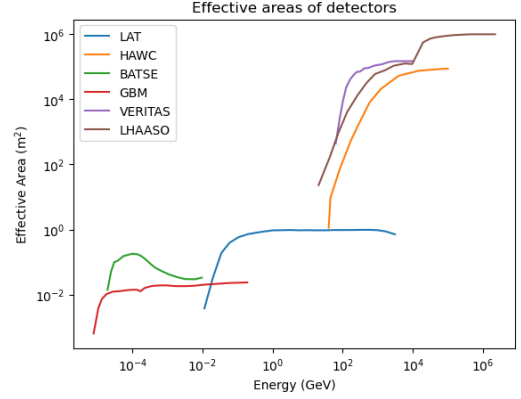
Figure 1.5: Effective areas of the detectors used in this work. We assume that photons outside given the described energy ranges are not detected (as in, $A_{\text{eff}} = 0$). More discussion in **section 2.2** and **Table 1.1** [45][46][43][37][48][22][12]

Table 1.1: Sensitivity metrics employed for each detector.

Detector	Angular sensitivity $d\Omega$	ζ_γ separation
Burst and Transient Source Experiment (BATSE)	10^{-3} [43]	-
Fermi Gamma-ray Burst Monitor (GBM)	10^{-3} [37]	-
Fermi Large Area Telescope (LAT)	10^{-3} [45]	-
High Altitude Water Cherenkov Observatory (HAWC)	10^{-5} [46]	10^{-2} [24] [42]
Very Energetic Radiation Imaging Telescope Array System (VERITAS)	10^{-5} [22]	10^{-1} [29]
Large High Altitude Air Shower Observatory (LHAASO)	10^{-4} [12]	10^{-5} [38]

10

1.6 This work

The goal of this work is to explore constraints on the direct-detection an evaporating black hole. This includes an overview of detection limits and the effects of known constraints, such as galactic dispersion and population density, and theoretical elements such as dark particle radiation and γ-ray afterglow. We explore these constraints in the γ-ray band, employing several observatories including the *Fermi*, HAWC and LHAASO missions as shown in **Figure 1.5**. We characterize PBH evaporation with several novel parameters that can be used to efficiently differentiate PBHs from other like γ-ray sources.

We find strong constraints for the detection limits of PBH γ-ray sources. We investigate two domains: γ-ray bursts in late-stage evaporation and long-term γ-ray source with monotonically increasing flux. Using the *Fermi* Large Area Telescope and Gamma-Ray Burst Monitors, we apply these constraints and analyze the resulting candidates using a combination of spectral and lightcurve modelling techniques.

Chapter 2

Viability for direct-detection of a PBH

2.1 Photon lightcurve parameterization

Starting as we did before in **equation 1.3** with the mass evolution $\frac{dM}{dt}$ and degrees of freedom $\alpha(M)$,

$$\frac{dM}{dt} \propto \frac{\alpha(M)}{M^2}, \tag{2.1}$$

$$M^3(t) \simeq M_0^3 - 3\alpha(M)t \tag{2.2}$$

The primary direct-emission spectrum of photons is well-understood due to its relationship with the temperature of the black hole. As discussed in **section 1.4**, the secondary fragmentation spectrum is not. We consider QCD confinement at ~ 200 MeV and begin with parameterization of the lightcurve first as it evolves in primary.

Primary emission is expected to be highly regular. We show that it is well-parameterized by a simple powerlaw of index $\beta < 0$. The particular value of this index is generally agnostic to the particular energies $E_\gamma \lesssim \mathcal{O}(10^{-2})$ GeV in which the signal
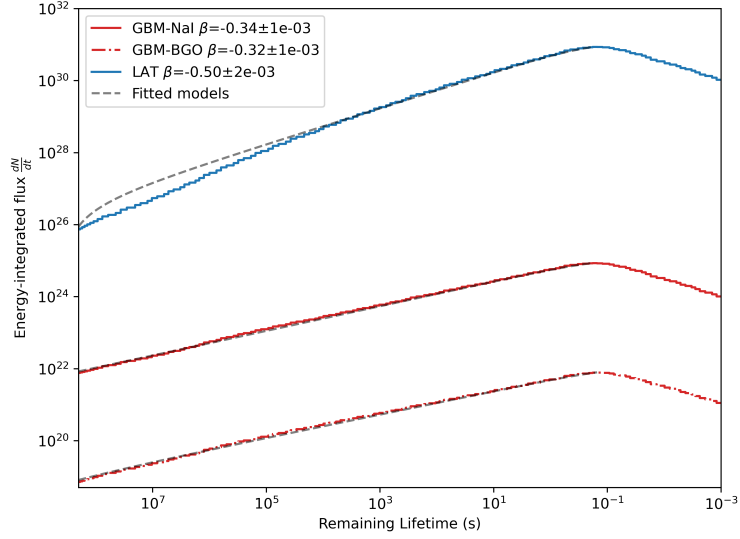
Figure 2.1: Fitting of parameterized powerlaw on data collected using BlackHawk hadronization simulation. Results are consistent with similar parameterizations of the PBH lightcurve near QCD confinement [51][35]. Note that the fitting interval extends only to the peak flux $\sim 10^{-1}$s, as the break thereafter is possibly non-physical [7].

is observed.

Given an absolute time T_0 at which evaporation concludes, we can define the lifetime as $\tau = T_0 - t$ which, plugging into **equation 2.2**, gives

$$M^3(\tau) \simeq M_0^3 - 3\alpha(T_0 - t) = M_0^3 - 3\alpha\left(\frac{M_0^3}{\alpha} - \tau\right) = 3\alpha\tau$$

$$M(\tau) \propto \tau^{1/3}$$

$$\phi_\gamma(\tau) \propto \frac{1}{M(\tau)} \propto \tau^{(-1/3)} \tag{2.4}$$

Noting again that this approximates $E_\gamma \lesssim 100$ MeV generally well. For energies exceeding this threshold, we rely on modelling approaches for QCD. In the case of 300 MeV to 100 GeV we use the parameterization $\dot{N}_\gamma \simeq 1.4 \times 10^{29} \left(\frac{T_{\mathrm{BH}}}{\mathrm{TeV}}\right)^{1.6}$ s^{-1} [35].

13

Following from **equation 2.4**,

$$\frac{1}{M(t)} \propto \left(\frac{T_{\mathrm{BH}}}{\mathrm{TeV}}\right) \simeq \left(\frac{485 \text{ s}}{\tau}\right)^{1/3}$$

(2.5)

$$\dot{N}_\gamma \simeq 3.8 \times 10^{30} \tau^{-0.53} \text{ s}^{-1}$$

This result is consistent with other parameterizations for the fragmentary PBH

lightcurve beyond hadronization. Ukwatta, et. al. [51] corroborates the powerlaw

approximation for $\beta = -0.52$ for energies $> 50\mathrm{GeV}$.

We model also with BlackHawk [5][6], a simulation of fragmentation using the

Pythia high-energy collision event generator [47][23]. We investigate β specifically for

the energy ranges of the *Fermi*-LAT and GBM detectors (not factoring in sensitivity).

We fit the powerlaw shape using simple regression and find that it well-approximates

the BlackHawk results. We show in **Figure 2.1** that both GBM detectors are near $\beta \sim$

$-1/3$, whereas the LAT results in $\beta = -0.50$. As such, we assume going forward that

detectors sufficiently beyond QCD confinement will generally follow the GeV-dominant

result from **equation 2.5**.

We therefore generalize the parameterized photon flux for an observed direct-

detection of an EBH to be,

$$F_\gamma \simeq K \times \tau^\beta \text{ cm}^{-2}\text{s}^{-1}$$

(2.6)

$$\text{for } K = 3.2 \times 10^{-8} \left(\frac{\mathrm{pc}}{d}\right)^2 \text{ cm}^{-2} \text{ and } \beta = -0.53$$

We expect for the incoming signal to be qualitatively "clean," meaning that

there are few deviations from the powerlaw shape. Multiple clear emission peaks, for

example, are more attributable to neutron star mergers [50]. Deviations from this pattern include the possibility for additional dark degrees of freedom affecting $\alpha(M)$ (discussed in **section 2.4**) and the possibility for a high energy, short time-lag afterglow (**section 2.5**).

2.2 Maximum possible distance for direct-detection

We choose to model a wide variety of high-energy telescopes, covering a range of energies nine order of magnitudes across in which photons from evaporating PBHs might be detected.

Beginning from the lowest energy ranges, the BATSE and its spiritual successor the *Fermi*-GBM are non-imaging scintillation detectors. Being satellites, they have a nearly all-sky field of view occulted only by Earth. In particular, the GBM has two sets of detectors spanning the entire keV energy range: the two opposing Bismuth Germanate (BGO) higher-energy and ten angularly distributed Sodium Iodide (NaI) lower-energy detectors [37]. The GBM overlaps with its partner instrument, the large-area imaging telescope *Fermi*-LAT which also boasts a large ≥ 70 degree field of view and spans the MeV-GeV range [45].

VERITAS is a ground-based mission intended to compliment *Fermi* by spanning the GeV and TeV ranges [22]. The telescope takes advantage of Cherenkov radiation air showers cascaded by cosmic rays or γ-rays interacting with Earth's atmosphere. This indirect method allows for the telescopes' effective areas to be orders of magni-

tudes larger than is possible with conventional imaging detectors. The HAWC [46] and LHAASO [12] missions scale the detection area at higher altitudes, with the latter sensitive to $\gtrsim$PeV photons.

The detection likelihood of a single PBH then boils down to the number of photons detected and suppression of background.

First, we require that the number of signal photons $N_S \geq 10$. These signal photons are scaled by the effective area A_{eff} (**Figure 1.5**), the angular resolution $d\Omega$ (**Table 1.1**) and the total observation time T_{obs}. We choose this minimum photon count in reference to the all-sky 5σ point source threshold limit for the *Fermi* mission [45]. Other detectors often require fewer photons per detection, though this signal reconstruction is dependent on the photon energy and γ-hadron separation, covered next. We therefore consider ≥ 10 photons to be a sufficiently conservative limit.

Our second criterion requires a meaningful signal-to-noise ratio over background photons N_B of 5σ, i.e. $N_S/\sqrt{N_B} \geq 5$. Background photons come from the standard isotropic γ-ray background and other misidentified cosmic rays, which we model with $\phi_B(E \gtrsim \text{MeV}) = 1.4 \times 10^{-6} \left(\frac{\text{E}}{\text{GeV}}\right)^{-2.1} \text{cm}^{-2}$ [33]. Cherenkov telescopes (HAWC, LHAASO, VERITAS) are sensitive also to cascades produced by cosmic rays, meaning that γ-ray detection is dependent on the efficiency of hadron background suppression ζ_γ (**Table 1.1**). This suppression is dependent on the photon energy, described by $\phi_{\text{sep}}(E) = 1.2 \times 7900 \times 10^{-4} \times \zeta_\gamma E^{-0.265}$ [38]. In this case, we take the strongest constraint from either the background or the hadron suppression: $max(\phi_B(E), \phi_{\text{sep}}(E))$.

For the purpose of modelling the spectral evolution, we employ the parame-

16

terized broken powerlaw model from Ukwatta, et. al. [51].

$$\phi(E_\gamma, T_{\mathrm{BH}}) = \begin{cases} 9 \times 10^{35} \left(\frac{1}{E_\gamma}^3\right) & E_\gamma \geq T_{\mathrm{BH}} \\[3mm] 9 \times 10^{35} \left(\frac{1}{T_{\mathrm{BH}}}\right)^{1.5} \left(\frac{1}{E_\gamma}\right)^{1.5} & E_\gamma < T_{\mathrm{BH}} \end{cases} \tag{2.7}$$

Assuming that the source is sufficiently close to be visible, we expect that a transient object can be associated over the course of a full year. It should be noted that this is an optimistic constraint, as it approximates the telescopes' respective sky coverage ability to associate a transient source over long lifetimes, as we will discuss in **section 2.4**. We expect the signal duration $T_{\mathrm{obs}} = min(1\mathrm{yr}, \tau)$ for a minimum 1 year or the remaining PBH lifetime; whichever is smaller.

With **equations 1.1, 2.5** relating T_{BH} to mass and lifetime τ, we can calculate the number of signal photons.

$$N_S(T_{\mathrm{BH}}, d) = \frac{T_{obs}}{\tau} \int dE \frac{d^2 N}{dt dE}(E, T_{\mathrm{BH}}) \times \frac{A_{eff} \Delta\Omega(E)}{4\pi d^2} \tag{2.8}$$

$$N_B(T_{\mathrm{BH}}) = \tau \times \int dE \ A_{eff}(E) \Delta\Omega(E) \times \begin{cases} \phi_{\mathrm{sep}}(E) & \zeta_\gamma > 0 \\[3mm] \phi_B(E) & \text{else} \end{cases} \tag{2.9}$$

Positive detection limit: $min(N_S \geq 10, \frac{N_S}{\sqrt{N_B}} \geq 5)$ (2.10)

We apply these constraints and show the maximmal distance curves as a function of lifetime and mass in **Figure 2.2**. Right away, we can see that the LHAASO observatory stands the best chance of PBH direct-detection, sporting a distance limit nearly a full order of magnitude larger than its peers. For both LHAASO and its runner-up the *Fermi*-LAT, we can imagine observing a transient source in the GeV

17
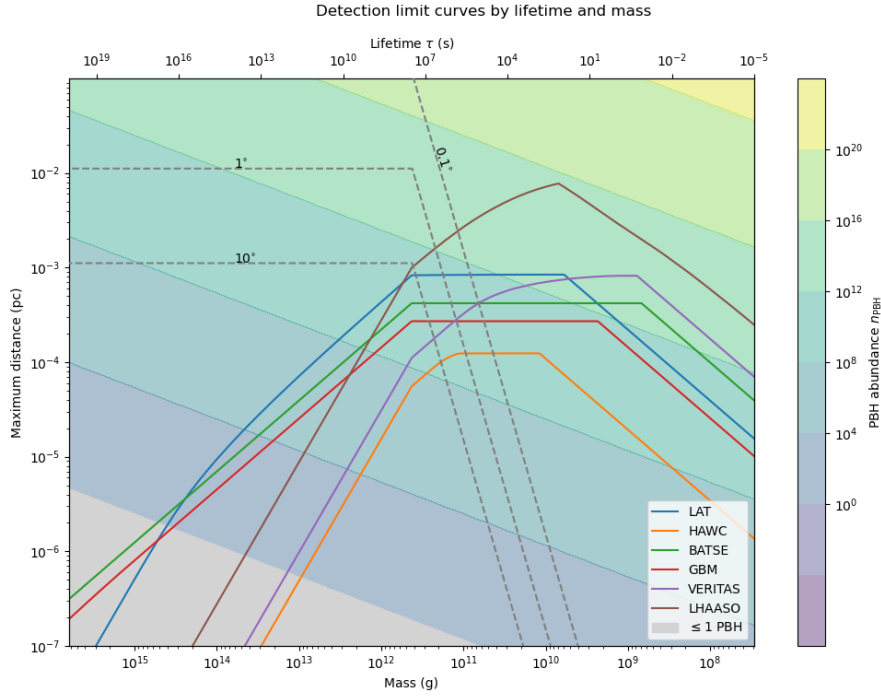
Figure 2.2: Maximum visible distance curves with respect to black hole mass for a number of modern γ-ray detectors as dictated by their respective effective area and angular resolution.

range, which monotonically increases over the course of a decade. Detection curves for the GBM currently underestimate background dominance for variable transient sources [30]. Pending the deployment of long-term GBM data processing pipelines, we can expect for late-stage black hole evaporation to be detected as a $\lesssim 1$s γ-ray burst (GRB). Both BATSE and GBM boast the wide sky-coverage necessary to detect PBH explosions, and the former has indeed been the subject to searches in the short-GRB domain [18].

2.3 Expected population density and isotropy

Given that the maximum detection distance for a PBH is less than a parsec (for reference, $<$ the size of the Oort cloud), we can safely assume that any number of detected explosions will be distributed according to the local dark matter distribution, i.e. distributed isotropically.

Using the local dark matter density $\rho_{DM} \simeq 0.4\,\text{GeV cm}^{-3}$ [14], we can calculate the number density of PBHs evolving from some initial mass function $\psi_i(M_i)$,

$$\frac{dn_{\text{PBH}}}{dM} = \frac{dn_{\text{PBH}}}{dM_i}\frac{dM_i}{dM}$$
$$\frac{dn_{\text{PBH}}}{dM_i} = \frac{\psi_i(M_i)}{M_i} \tag{2.11}$$

Using **equation 2.2**, we calculate $\frac{dM_i}{dM} = \frac{d}{dM}\left(M^3 + 3\alpha(M)t\right)^{1/3} = \frac{M^2}{M_i^2}$. Then,

$$\frac{dn_{\text{PBH}}}{dM} = \psi(M_i)\frac{M^2}{M_i^3} \tag{2.12}$$

PBHs which are exploding in current day will have mass $M = 0$, leaving $M_i|_{M=0} = 3\alpha(0)t$. Using **equation 1.1** and allowing ρ_{PBH} to be the PBH mass density,

$$\dot{n}_{\text{PBH}} = \frac{dn_{\text{PBH}}}{dM}\left(-\frac{dM}{dt}\right) = \psi_i(M_i)\frac{M^2}{M_i^3}\left(\rho_{\text{DM}}\frac{\alpha(M)}{M^2}\right)\bigg|_{M=0}$$
$$\dot{n}_{\text{PBH}} = \rho_{\text{DM}}\psi_i\left((3\alpha(0)t)^{1/3}\right)\frac{1}{3t} = \rho_{\text{DM}}\frac{\psi_i(M_U)}{t_U} \tag{2.13}$$

for age of the universe $t_U = 13.7\text{Gyr}$ and $M_U = 3\alpha(0)t_U = 5 \times 10^{14}\text{g}$.

The burst rate density is dependent on the chosen initial mass function. One rudimentary example is a monochromatic mass function $\psi_{\text{mono.}}(M) = f_{\text{PBH}}(M_U)\delta(M - M_U)$ [14][16]. Number density today is with respect to isotropic distance d is simply,

$$n_{\text{PBH}}(d) = \rho_{\text{DM}}f_{\text{PBH}}\frac{4}{3}\pi d^3 \tag{2.14}$$

19

Shown as the contour background of **Figure 2.2**, the number density using the monochromatic mass function with $f_{\text{PBH}} = 1$ would allow for PBHs to be abundant for to a variety of modern γ-ray detectors. Note that the monochromatic mass function is a generally unrealistic approximation to the expected formation mechanisms for PBHs (**section 1.3**). We imagine this monochromatic distribution generally as a description of abundance scaling with distance and PBH lifetime, acknowledging also the relatively narrow distribution that PBHs can occupy.

We can calculate that width with the log-normal mass function,

$$\psi_{\text{log}-\text{norm}}(M) = \frac{exp(-\log^2(\mathrm{M/M_U})/2\sigma^2)}{\sqrt{2\pi}\sigma M}$$

$$\dot{n}_{\text{PBH}} = \Gamma_{\text{PBH}} n_U \simeq \frac{8.5 \times 10^{-3}\text{pc}^{-3}\text{yr}^{-1}}{\sigma}$$

(2.15)

Recent limits placed by the HAWC observatory restrict the number of PBH explosions in the current epoch per unit volume to $\leq 3400\text{pc}^{-3}\text{yr}^{-1}$ [1], giving us $\sigma \sim 10^{-6}$. Combined with f_{PBH}, this result restricts the mass range to a very small corridor around M_U. For this reason, we consider for our needs the monochromatic mass function to be sufficient approximation.

2.4 Effect of proper motion

Given such strong constraints on the proximity for an EBH, we cannot neglect the effect of proper motion on our ability to accurately track a γ-ray source [32]. We can estimate the worst-case scenario by imagining that all velocity from the average galactic dispersion is transverse $v_T = v \approx 200$ km s^{-1} [8] (also evident in **Figure 1.1**).

The proper motion as a function of distance d, lifetime τ and maximum observation window T_{obs} we describe,

$$\theta = \frac{180°}{\pi} v_T \times \frac{min(\tau, T_{\text{obs}})}{d} \tag{2.16}$$

At 0.01 parsecs we get roughly 1 degree per year. This jumps beyond 10 degrees per year at 0.001 parsecs.

Of course, two factors tune the effect of proper motion. First, the magnitude of the velocity components directed radially or transverse. The visibility of sources moving purely radially (directly to/away from us) is handled in the subsequent section as it pertains to its effect on luminosity. Second, the ability for modern γ-ray detectors to associate sources as they trace relatively large distances across the sky. Especially with transient sources of low signal to noise, the choice of algorithm [31] and variance in the γ-ray background [30] can constrain detection at $\lesssim 1$ degree per year.

We include the corresponding contour lines for 0.1, 1 and 10 degrees of proper motion as they constrain the likelihood for detection in **Figure 2.2**. We consider it highly unlikely for a transient source to be detected in the ≥ 10 degree domain.

2.5 Effect of motion on luminosity

Considering the opposite case, the majority of speed from the galactic dispersion may be radial, such that the source is moving *away* from Earth at $v_r \approx 200$ km s^{-1} [8]. Suppose that a source is observed at distances d_1, d_2 at corresponding times $\tau - t_1$, $\tau - t_2$ such that $\Delta t = t_2 - t_1 = 1$ year, and therefore $d_2 + d_1 = v(t_2 - t_1) = v\Delta T_{\text{obs}}$.

Assuming a powerlaw dependence of the luminosity on the remaining PBH lifetime, $L_\gamma \propto \tau^\beta$, and setting $t_1 = 0$, the ratio of fluxes for $[\tau, \tau - T_{\text{obs}}]$ is

$$\frac{L_2}{L_1} = \left[\frac{\tau}{\tau - T_{\text{obs}}}\right]^\beta \left(\frac{d_1}{d_2}\right)^2 = \left[\frac{\tau}{\tau - T_{\text{obs}}}\right]^\beta \cdot \left[\frac{d_1}{d_1 + vT_{\text{obs}}}\right]^2 \tag{2.17}$$

We would expect the strongest luminosity suppression to occur at close distances or late stage evaporation, when the proportional effect of motion is strongest. In the worst-case scenario that all motion is directed away from Earth ($T_{\text{obs}} \times v$), taking as is usual $T_{\text{obs}} = 3 \times 10^7$s and $\beta = -1/3$, we expect luminosity suppression at our maximal detection distance $\leq 10^{-2}$pc to be $\frac{L_2}{L_1} \sim 10^{-10}$. As such, we consider the effect of luminosity suppression to be effectively negligible.

2.6 Spectral energy index

Outside of the high regularity of the PBH lightcurve, we can also look at the spectral evolution of a PBH. We know from **Figure 1.3** that PBH temperature dictates the evolution of photon energy. As we know from **equation 2.7**, the energy spectrum is well-described by a broken powerlaw. We can model the evolution of temperature by finding the spectral index evolution about a given pivot energy as it evolves with time.

Suppose we have an arbitrary flux normalization K and the spectral powerlaw index γ [31].

$$\phi(E) = K \left(\frac{E}{1 \text{ GeV}}\right)^{-\gamma} \tag{2.18}$$

We can find γ by solving the slope around the pivot energy E. We approximate this simply by taking two fluxes $\phi_1(E_+)$, $\phi_2(E_-)$ where $E_+ - E_-$ is small. Taking the log of

22
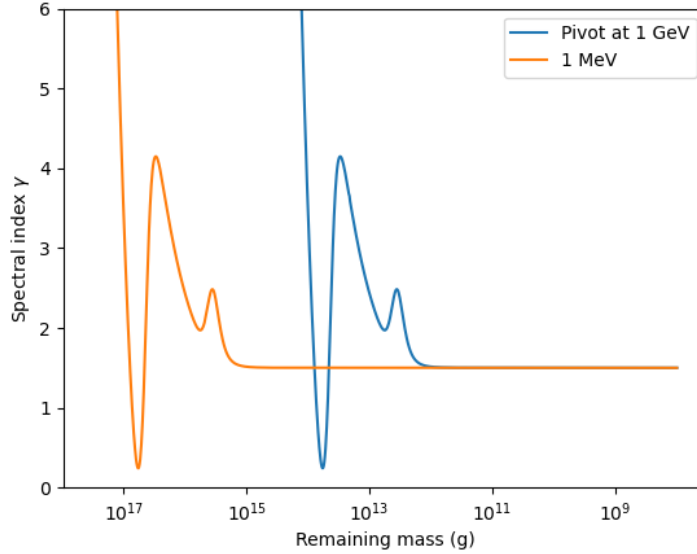
Figure 2.3: Spectral powerlaw index γ at 1 GeV and MeV as a function of mass. This illustrates the evolution of the energy spectrum with black hole temperature as $T_{\mathrm{BH}} = 1$ GeV and 1 MeV at PBH masses of $\sim 10^{13}$g and $\sim 10^{16}$g respectively.

each equation and subtracting, we can derive

$$\log(\phi_1) - \log(\phi_2) = -\gamma(\log(E_1) - \log(E_2))$$
$$\gamma = \frac{\log(\phi_2/\phi_1)}{\log(E_1/E_2)} \tag{2.19}$$

We use the more-detailed parameterization of time-evolved spectrum as derived by Ukwatta et. al. [51]. The evolution of γ for pivot energies 1 GeV and 1 MeV are shown in **Figure 2.3**. This is an excellent visualization of the temperature-energy relationship for EBH photon spectrum. Exceeding $\tau \gtrsim 10^5$ s, the spectral index for 1 GeV is large, reflecting the $\ll$GeV emission at low temperature. The MeV line follows the exact same shape, but precedes the GeV line as its energy is reached earlier in the BH lifetime. In both cases, the γ approaches -1.5 at lifetimes $\lesssim 10^5$s.

23

2.7 Advantages in multi-mission detection

We can take advantage of these aforementioned spectral characteristics, should a signal be observed in more than one high-energy detector. Considering specifically a pair-trigger system such as the LAT and GBM (whose constituent detectors NaI and BGO each have different energy ranges), the cumulative flux will proceed first in the lower-energy detectors and later in the higher-energy detector.

In fact, this timing of peak flux is another metric by which we can identify EBH signatures in a multiple-detector observation scenario. We expect for lower-energy detectors' peak flux to transpire before that of the higher-energy detectors. This time delay is nominal for the LAT and GBM detectors due to the large overlap in their energy ranges (in the region of 10^{-1}s).

In the event of a multi-mission detection, one energy range may not resemble a PBH signal so much as others – as we'll discuss in the subsequent section, a sign of changes in radiation degrees of freedom α at certain temperatures. As such, time-resolved broadband spectral analysis would be the most promising means to discern radiation products beyond the Standard Model [52].

2.8 Effect of additional dark degrees of freedom

Outside of some unknowns in the hadronization stage of PBH evaporation, we can also consider the evaporation of a PBH into undiscovered dark degrees of free-dom. These dark particles would not fragment into light emissions and would therefore

transform the otherwise predictable powerlaw shape of the lightcurve.

Suppose there are additional dark degrees of freedom which modify the evaporation rate $\alpha \to \alpha + \alpha_D$ at some time t_D. Following the initial mass evolution $(t > t_D)$ in **equation 2**,

$$M^3_{t>t_D}(t) = M^3_0 - 3\alpha(t_D) - 3\alpha_D(t - t_D) = M^3(t) - 3(\alpha - \alpha_D)(t - t_D) \qquad (2.20)$$

Therefore the lightcurve $\phi_\gamma(t)$ at time $t > t_D$, allowing that $\Delta\alpha = \alpha_D - \alpha$ (and noting that $\alpha_D > \alpha$) is

$$\phi_\gamma(t) \to \phi_\gamma\left(t + \frac{\Delta\alpha}{\alpha}(t - t_D)\right) \qquad (2.21)$$

Let's redefine time as the time to evaporation τ with respect the absolute explosion time T_0. Then $\tau = T_0 - t$ and $\tau_D = T_0 - t_D$,

$$\phi_\gamma(\tau) = \phi_\gamma\left(\tau + \tau\frac{\Delta\alpha}{\alpha}\right) \text{ for } \tau < \tau_D$$

$$\phi_\gamma(\tau) = \phi_\gamma\left(\tau + \tau_D\frac{\Delta\alpha}{\alpha}\right) \text{ for } \tau \geq \tau_D$$

$$(2.22)$$

We visualize the effect of dark particle radiation in **Figure 2.4** using the simple parameterized powerlaw (**equation 2.6**), comparing the ordinary lightcurve and the dark lightcurve with several values for $\Delta\alpha/\alpha$. As expected, dark sector evaporation reduces the total number of photons emitted in the EBH lifetime. Timescale τ_D and its magnitude $\Delta\alpha/\alpha$ tune the degree to which this suppression occurs. Using the same parameters, we show the ratio of fluxes – the dark sector lightcurve divided by the ordinary lightcurve, to visualize this deviation over time. Shown in **Figure 2.5**, we see that at late lifetimes, large values of $\Delta\alpha/\alpha$ can diminish the peak flux by orders of magnitude.

In the event that a PBH explosion with dark particle radiation is observed, we can parameterize α_D in the following way.

$$\frac{\phi_\gamma^{\mathrm{DS}}(\tau_D)}{\phi_\gamma(\tau_D)} = \frac{K\left(\tau_D + \tau_D \frac{\Delta\alpha}{\alpha}\right)^\beta}{K\tau_D^\beta}$$

$$\phi_\gamma^{\mathrm{DS}}(\tau_D) = \left(1 + \frac{\Delta\alpha}{\alpha}\right)^\beta \phi_\gamma(\tau_D)$$

(2.23)

Normalization and the timescale for τ_D fall out, meaning that the dark sector lightcurve $\phi_\gamma^{\mathrm{DS}}(\tau_D)$ depends only on a factor of $\Delta\alpha/\alpha$.

If $\Delta\alpha/\alpha$ is not very large, the effect on the lightcurve may be too small to detect. In the event of a PBH signal, we can determine the detection limit for the dark sector photons by applying the same approach outlined in **section 2.2** Taking the coefficient in **equation 2.21**, we can assume a dark sector signal N_S^{DS} and calculate both constraints $N_S^{\mathrm{DS}} > 10$ and $N_S^{\mathrm{DS}}/N_B > 5$. We show for the LAT at a distance 10^{-4}pc the signal significance for a dark sector lightcurve in **Figure 2.6**. Note that as N_S^{DS} scales with $\frac{(1+\Delta\alpha/\alpha)^\beta}{d^2}$, we can know that in general, the distance limit for detection $d \propto (1 + \Delta\alpha/\alpha)^{\beta/2}$.

2.9   Dependence of signal duration on parameterized index

The duration of a detected signals in γ-ray bursts is often characterized with respect to its t_{90} and t_{50} corresponding to the time intervals in which 90% and 50% of the total signal flux is detected. This characteristic can be exploited as a proxy for the PBH lightcurve index β.

Consider the end of a PBH γ-ray signal as it is observed by a detector to be t_0.

26
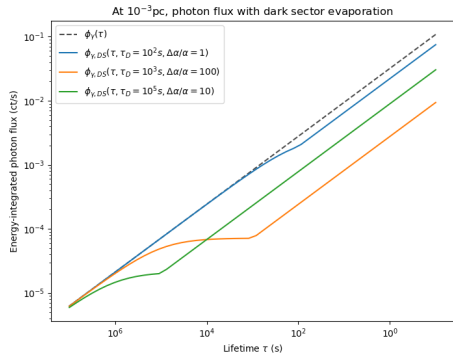
Figure 2.4: Lightcurves as compared with ($\phi_{\gamma,\mathrm{DS}}$) and without ($\phi_\gamma$) dark sector evaporation. As shown, $\Delta\alpha/\alpha$ defines the magnitude to which the lightcurve deviates from known physics, whereas τ_D tunes its timing.
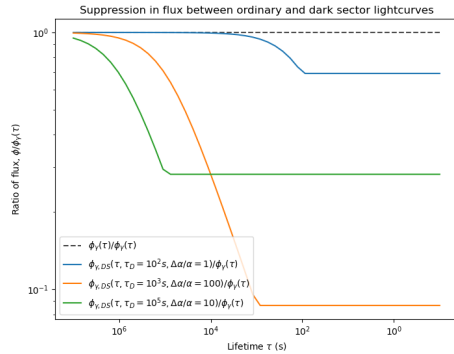
Figure 2.5: The ratio of the dark sector lightcurves to the ordinary lightcurve, mirroring the parameters of **Figure 2.4**. The dashed line represents the ordinary case at 1. We can see the effect of suppression at peak flux by $\Delta\alpha/\alpha$ and the suppression of total fluence (time-integrated flux) by τ_D.
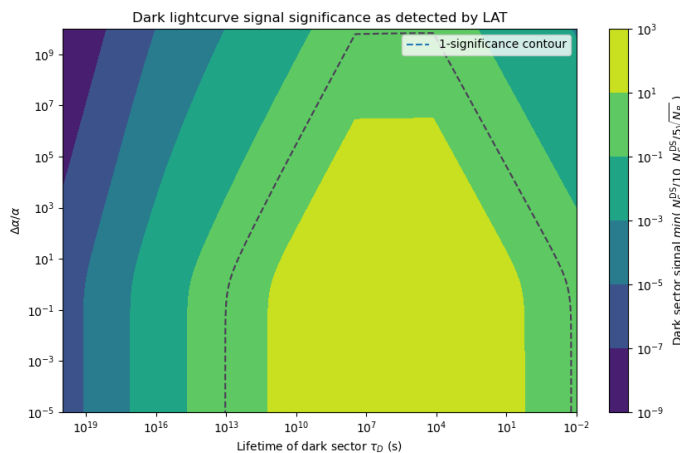
Figure 2.6: For the Fermi-LAT detector at a distance of 10^{-4}pc: the effect of variations in $\Delta\alpha/\alpha$ on the signal significance $min(N_S^{\mathrm{DS}}/10, N_S^{\mathrm{DS}}/5\sqrt{N_B})$. In the limit of $\Delta\alpha/\alpha = 0$, there are no dark sector degrees of freedom. In contrast, one can see the suppression of photons in large $\Delta\alpha/\alpha$. The decline at small values of τ_D is due to the LAT's decline in A_{eff} at $E \gg TeV$. We show the 1-significance contour (dashed black) corresponding to the threshold at which we could detect the dark sector.

27

This obviously coincides with the expiration of the PBH at lifetime $\tau = 0$. Noting from the results of **Figure 2.2**, we can see that the downturn in photon sensitivity occurs within a small timescale. Compared to T_{obs}, this difference is effectively negligible – $\lesssim 1$s for the GBM.

Suppose a signal arrives with true duration t_{100}. We can find the total fluence to be $\propto \int_0^{t_{100}} \tau^\beta d\tau$ for the parameterized lightcurve τ^β (with $\beta < 0$ but $|\beta| < 1$). Therefore, the 90% threshold requires

$$\int_0^{t_{90}} \tau^\beta d\tau = 0.9 \int_0^{t_{100}} \tau^\beta d\tau$$

$$(\beta + 1)ln(t_{90}) = ln(0.9) + (\beta + 1)ln(t_{100}) \tag{2.24}$$

$$t_{90} = t_{100}(0.9)^{\frac{1}{\beta+1}}$$

We calculate $t_{50} = t_{100}(0.5)^{1/(\beta+1)}$ similarly. By ratioing these two components, we leave out t_{100}. Depending only then on the powerlaw index,

$$\frac{t_{90}}{t_{50}} = \left(\frac{9}{5}\right)^{\frac{1}{\beta+1}} \tag{2.25}$$

For temperature $\lesssim 100$ MeV we expect $\beta = -0.33$ which gives a value of $t_{90}/t_{50} = 2.4$. More realistically in the case of GRBs, we expect for $\beta = -0.53$, corresponding to $t_{90}/t_{50} = 3.5$. In the case of dark particle radiation, we can estimate that for large $\Delta\alpha/\alpha$, we expect $t_{90}/t_{50} \to 1$.

2.10   Possibility for afterglow

Recent confirmation of radio afterglows from hadronized neutron star merger products on the order of a few days following an initial GRB [49] suggest the possibility

that an EBH could produce a similar afterglow. There is some debate over whether the byproducts of an EBH could be optically thick [14]. An EBH afterglow would likely span multiple orders of energy and could be another example in which multi-spectral analysis greatly improves detection.

Since the timescale and luminosity of these EBH afterglows are essentially wide-open, it is technically possible that one or more afterglows could arrive during and/or after the initial direct-collapse emission of the PBH. This tentatively allows GRB candidates previously ruled out whose lightcurves show multiple peaks (e.g. **Figure 2.8**). It is possible also that the generally sharp drop-off after peak emission described by the previous section may also be broadened by an afterglow which occurs closely behind. The combined lightcurve and afterglow shape would be modelled as the direct sum of both [49].

$$\phi_\gamma(E) = K_1 \tau^\beta + K_2 \frac{e^{Ax}}{1 - e^{Bx}} \tag{2.26}$$

An example of this model fitted to a GRB is shown in **Figure 2.7**.

Composite Bayesian fit of bn150902733
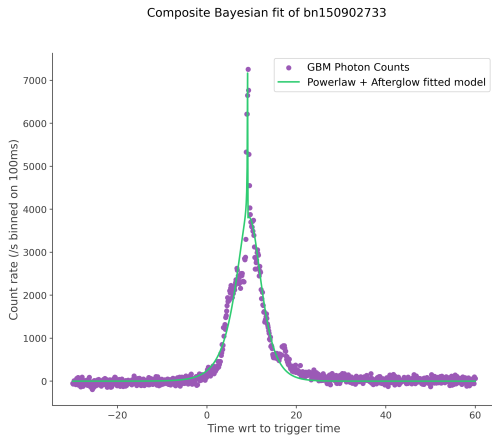
Figure 2.7: An example of afterglow broadening the shape of a signal. We average the photon counts of the four smallest-angle GBM detectors to bn150902733 and fit with a composite model which sums the contributions from a simple powerlaw and afterglow. Lightcurve retrieval and multiparameter fitting was performed using ThreeML [52].

Composite countrate of bn140206275
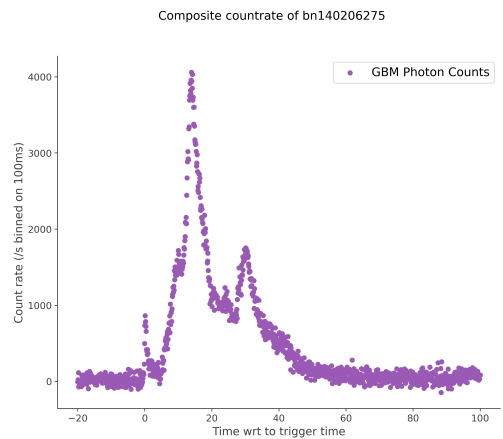
Figure 2.8: The average photon count for bn140206275, which contains multiple peaks which appear before and after largest emission peak. These secondary peaks are often associated with neutron star mergers [50], though it is still possible that the afterglow of a PBH could be responsible for these secondary peaks.

Part II

Searching for primordial black

holes in γ-ray source catalogs

Chapter 3

Introduction

The constraints derived in previous sections paint a strict picture for the possible domains in which a PBH could be detected by modern γ-ray detectors. We find that there are two general scenarios in which detection is possible.

In large lifetime and with sufficiently close distance, PBHs may be visible as a transient source. Of course, the largest issue in this domain is proper motion, meaning that we would favor transient γ-ray sources either with relatively brief lifetimes, or detected within a relatively small observation window. For the former, we can quickly calculate from the intersection of the 1-degree proper motion curve and the LAT maximal detection that $\tau \lesssim 2 \times 10^6$ is generally suited for detection. The effect of luminosity suppression should be negligible for detection constraints at this range, though it could disturb the expected lightcurve shape. As such, we are generally just looking for sources with motonically increasing flux. In this domain, we employ the **Fermi**-LAT for its catalog of transient sources. The *Fermi*-GBM would also have capability for tracking

long-term sources, however the dominance of variations in the γ-ray background over long timescales constrain analysis to ~ 1 min [30].

For this reason, there is good reason to believe that the GBM could detect a PBH at late stage evaporation as a GRB. Additional allowance can be made with the possibility of dark degrees of freedom at small τ_D that hinder detection at earlier lifetimes (**section 2.8**) or, less likely, significant luminosity amplification as the result of motion. We expect far greater abundance of PBHs in the domain of late-stage evaporation and high detection limit ($\gtrsim 10^{-4}$pc), adding to the value to investigating these GRBs.

GRB sources detected in this way should be visible to the LAT for a great deal longer than in the GBM, of course, on proximity and velocity. For this reason, we attempt also to associate candidate GRBs to previously-detected transient sources in the LAT.

3.1   Analysis of long-term γ-ray sources

In pursuit of long-term sources, we employ the LAT Transient Catalog [31]. This source catalog uses data collected from August 4th, 2008 to August 15, 2018 – over a decade of data. We looked for "unassociated" sources, labelled as such for weak correlation with any other known sources at other wavelengths. At the time of retrieval, we found lightcurves for 35 remaining unassociated sources.

We fit the lightcurve of these sources with the simple parameterized model in

equation 2.6. In this case, our two parameters are the proximity d and the lifetime at initial detection, T_0. We calculate the observation window T_{obs} and take it as the lower-bound of T_0. This value is shown in **Figure 3.1** as ΔMJD from the final and initial detection times respectively, is also useful in context with expected proper motion (<10 degrees per ~ 350 days). We leave the remaining bounds for d and T_0 open.

We treat each error of each datapoint as a Gaussian. We apply a nonlinear least squares regression to each lightcurve for the described model. The fitting process leaves wide errors for the model owing to the small sample size. We obviously neglect to fit sources with a single datapoint, but some sources have just one degree of freedom. For this reason, we independently calculate the standard error of the model and choose to proceed with the 50% confidence intervals as shown in **Figure 3.1**. The fitted parameters for each source are entered in **Table 3.1**. We can very clearly see the resulting effect of these errors when we plot these results in **Figure 3.2**, superimposed on the detection curves calculated previously. Spectral powerlaw index, shown in **Figure 3.3**, also provides weak constraints due to the wide errors in lifetime.

Some sources with high monotonic increase show positive signs for exploding in the near future, with a handful broaching timescales in the next century, yielding the possibility that maximal flux will improve signal significance for other telescopes. This would benefit multi-spectral investigation of long-term PBH candidates, provided the detection and tracking of transient sources in other wavelengths is feasible. To that effect, we attempt a rudimentary approach in **section 3.2** to associate these candidates with GRBs from the GBM monitor.

34
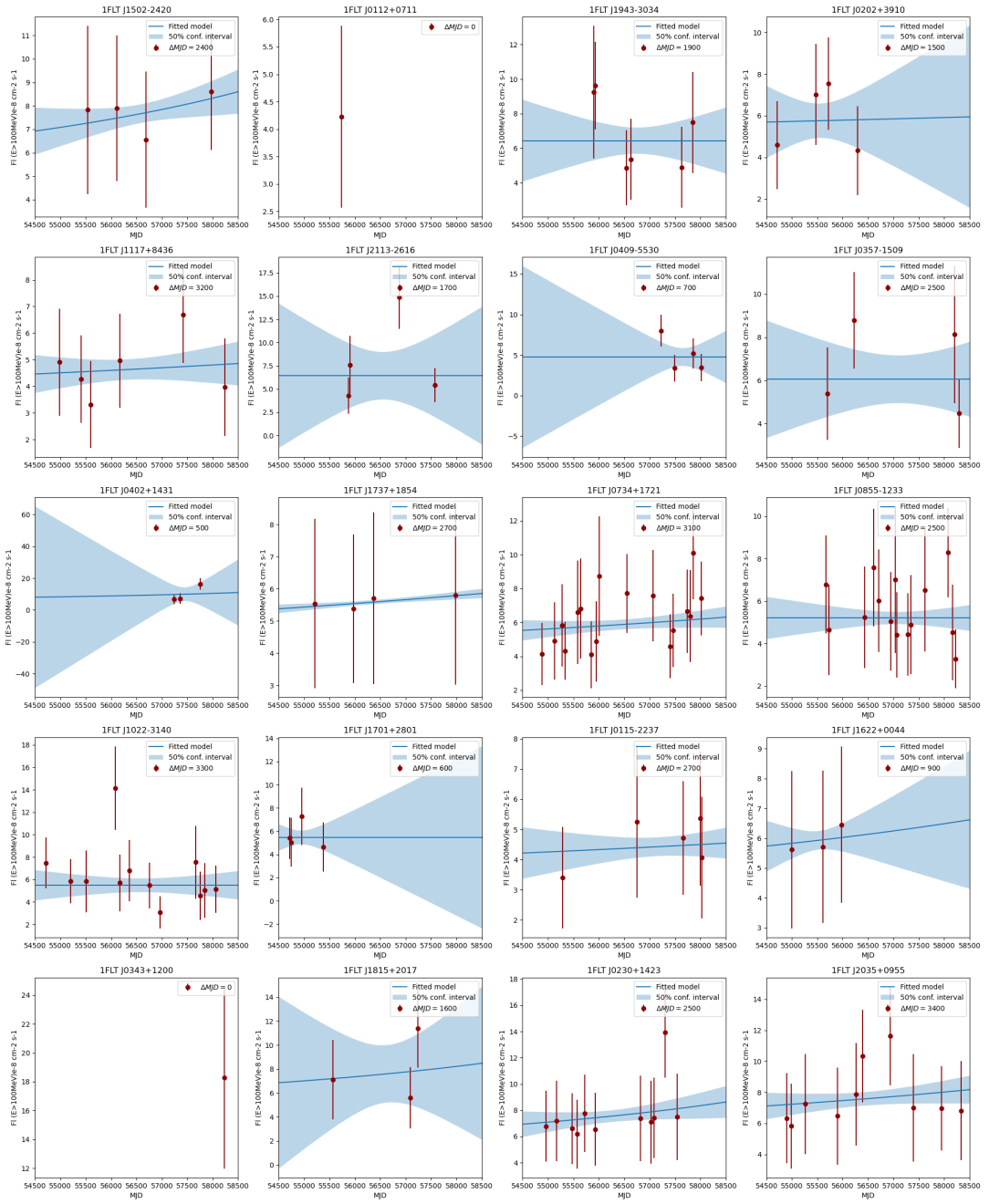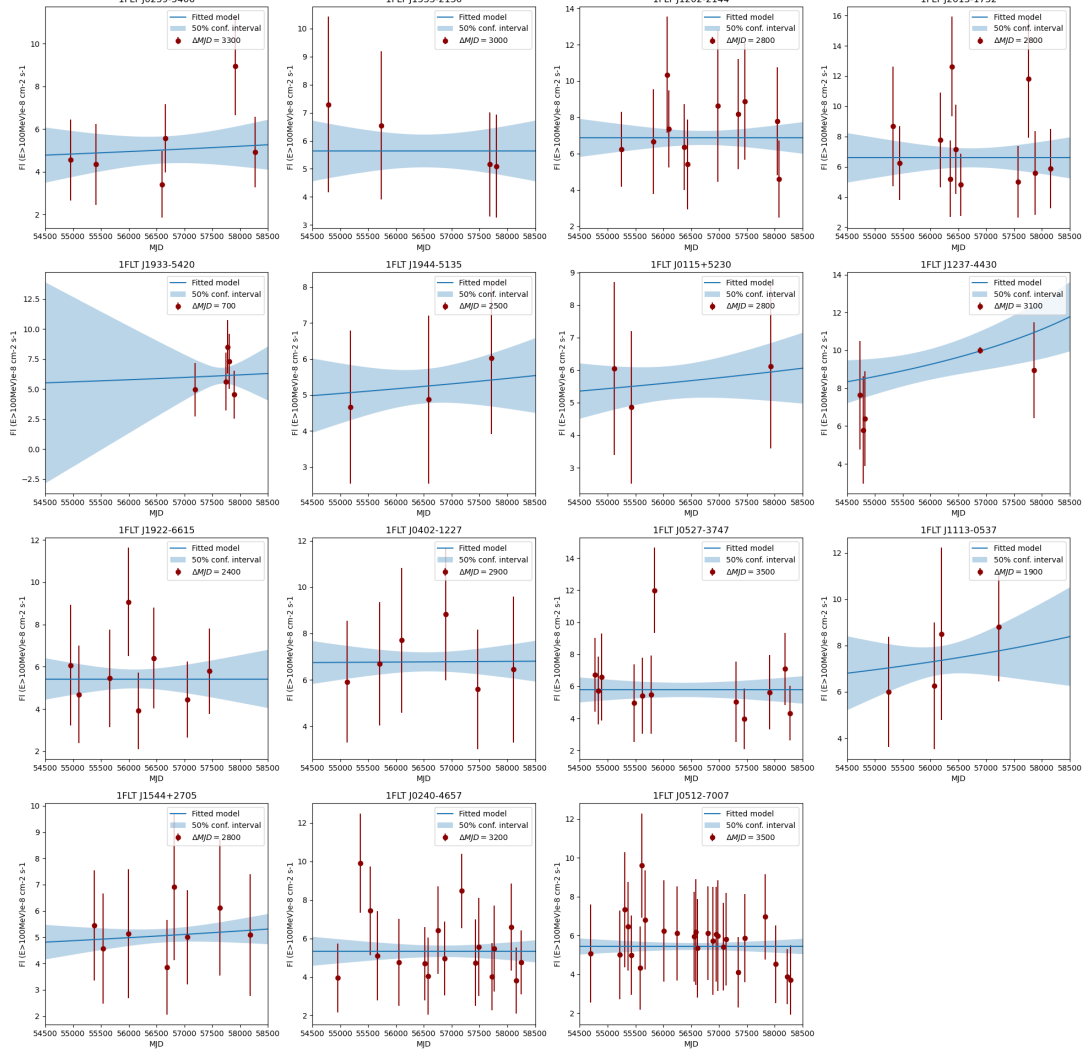
Figure 3.1: Parameterized powerlaw model (blue) with 50% confidence interval (blue shaded) applied to unassociated γ-ray transients detected by the *Fermi*-LAT (red errorbars). Duration of signal is shown for reference in Modified Julian Days $T_{\mathrm{obs}} = \Delta MJD$.

Figure 3.2: Transient fit results superimposed on the detection limits described in previous sections. Source 1FLT J2113-2616 omitted.

Figure 3.3: Lifetime and spectral index γ as fitted for the transient sources compared to the theoretical expectations for the same.

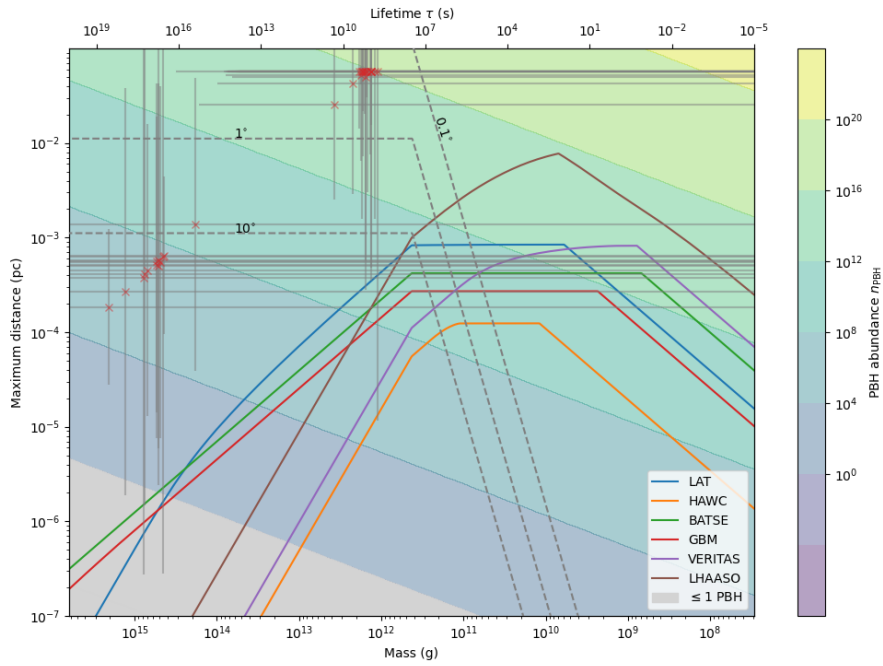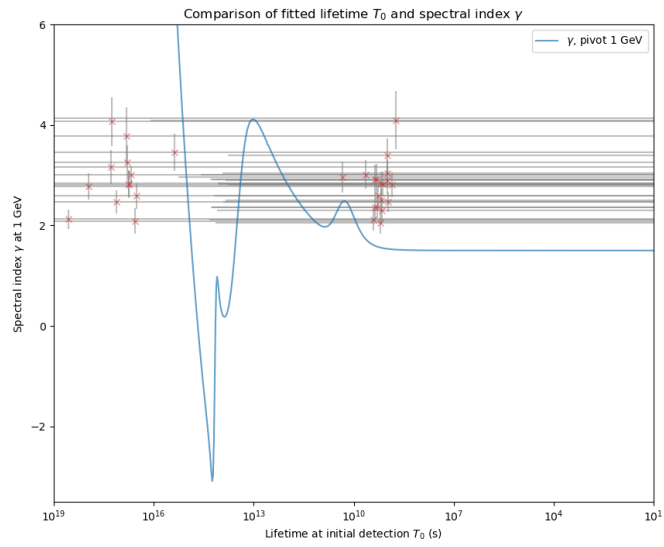| Source name	R.A. (deg)	DEC (deg)	T_0 (s)	T_0 upper lim. (s)	T_0 lower lim. (s)	d (pc)	d upper lim. (pc)	d lower lim. (pc)	γ	γ err.
1FLT J0112+0711	18.21	7.196	-	-	-	-	-	-	2.289	0.26
1FLT J0115+5230	18.858	52.515	1.61e+13	1.25e+14	2.08e+12	5.66e-02	1.57e-01	2.03e-02	2.058	0.225
1FLT J0115-2237	18.957	-22.63	2.55e+13	4.05e+14	1.60e+12	5.66e-02	2.25e-01	1.42e-02	2.12	0.223
1FLT J0202+3910	30.599	39.172	4.41e+13	9.57e+15	2.03e+11	4.23e-02	6.24e-01	2.87e-03	3.013	0.285
1FLT J0230+1423	37.638	14.393	9.84e+12	2.53e+17	3.83e+08	5.66e-02	9.07e+00	3.53e-04	3.388	0.352
1FLT J0240-4657	40.158	-46.951	5.67e+20	3.22e+25	1.00e+16	5.72e-04	1.36e-01	2.40e-06	2.842	0.264
1FLT J0259-5406	44.842	-54.103	2.03e+13	2.55e+16	1.61e+10	5.66e-02	2.01e+00	1.59e-03	2.922	0.3
1FLT J0343+1200	55.757	12.004	-	-	-	-	-	-	2.496	0.233
1FLT J0357-1509	59.404	-15.155	6.56e+20	8.76e+23	4.91e+17	5.17e-04	1.89e-02	1.41e-05	3.782	0.564
1FLT J0402-1227	60.511	-12.463	2.13e+14	2.22e+16	2.05e+12	2.56e-02	2.61e-01	2.51e-03	2.966	0.307
1FLT J0402+1431	60.664	14.522	5.39e+12	1.26e+20	2.30e+05	5.66e-02	2.74e+02	1.17e-05	4.095	0.585
1FLT J0409-5530	62.292	-55.503	2.44e+19	3.06e+22	1.95e+16	1.39e-03	4.93e-02	3.94e-05	3.456	0.364
1FLT J0512-7007	78.053	-70.129	9.21e+21	1.86e+26	4.55e+17	2.71e-04	3.85e-02	1.90e-06	2.774	0.266
1FLT J0527-3747	81.798	-37.793	1.77e+21	1.35e+26	2.32e+16	4.07e-04	1.12e-01	1.47e-06	4.066	0.487
1FLT J0734+1721	113.702	17.357	1.54e+13	6.17e+17	3.82e+08	5.66e-02	1.13e+01	2.82e-04	2.493	0.231
1FLT J0855-1233	133.753	-12.56	6.23e+20	3.48e+24	1.12e+17	5.65e-04	4.22e-02	7.56e-06	3.25	0.347
1FLT J1022-3140	155.738	-31.672	3.73e+20	1.93e+27	7.24e+13	6.30e-04	1.43e+00	2.77e-07	2.09	0.258
1FLT J1113-0537	168.362	-5.628	9.96e+12	5.51e+14	1.80e+11	5.66e-02	4.21e-01	7.61e-03	3.035	0.283
1FLT J1117+8436	169.283	84.615	2.31e+13	1.76e+15	3.02e+11	5.66e-02	4.95e-01	6.47e-03	2.918	0.293
1FLT J1202-2144	180.73	-21.735	5.63e+20	4.02e+24	7.87e+16	5.05e-04	4.27e-02	5.98e-06	2.813	0.271
1FLT J1237-4430	189.475	-44.507	7.03e+12	8.91e+15	5.55e+09	5.66e-02	2.01e+00	1.59e-03	2.807	0.247
1FLT J1502-2420	225.727	-24.339	9.38e+12	1.26e+14	6.97e+11	5.66e-02	2.07e-01	1.54e-02	2.462	0.191
1FLT J1533-2130	233.45	-21.503	3.67e+22	1.64e+24	8.21e+20	1.84e-04	1.23e-03	2.76e-05	2.123	0.192
1FLT J1544+2705	236.044	27.096	1.96e+13	1.20e+15	3.21e+11	5.66e-02	4.43e-01	7.23e-03	2.365	0.224
1FLT J1622+0044	245.713	0.742	1.42e+13	4.89e+13	4.13e+12	5.66e-02	1.05e-01	3.05e-02	2.302	0.252
1FLT J1701+2801	255.418	28.02	3.36e+20	1.54e+22	7.30e+18	6.50e-04	4.41e-03	9.58e-05	2.585	0.252
1FLT J1737+1854	264.27	18.903	2.27e+13	3.43e+13	1.50e+13	5.16e-02	6.34e-02	4.20e-02	2.36	0.268
1FLT J1815+2017	273.952	20.287	9.53e+12	1.34e+17	6.79e+08	5.66e-02	6.70e+00	4.78e-04	2.896	0.266
1FLT J1922-6615	290.608	-66.254	1.34e+21	1.66e+24	1.09e+18	4.52e-04	1.59e-02	1.29e-05	2.466	0.235
1FLT J1933-5420	293.423	-54.343	1.34e+13	4.59e+15	3.91e+10	5.66e-02	1.05e+00	3.06e-03	2.827	0.248
1FLT J1943-3034	295.91	-30.572	4.74e+20	2.47e+24	9.09e+16	5.46e-04	3.95e-02	7.56e-06	3.01	0.165
1FLT J1944-5135	296.122	-51.599	1.85e+13	1.23e+14	2.79e+12	5.66e-02	1.46e-01	2.20e-02	2.593	0.204
1FLT J2013-1732	303.499	-17.545	1.91e+21	3.45e+27	1.05e+15	3.73e-04	5.03e-01	2.77e-07	3.162	0.335
1FLT J2035+0955	308.903	9.924	1.48e+13	1.16e+17	1.89e+09	5.03e-02	4.45e+00	5.69e-04	2.838	0.236
1FLT J2113-2616	318.368	-26.269	4.58e+31	7.67e+38	2.73e+24	6.71e-07	2.75e-03	1.64e-10	4.141	0.578

Table 3.1: γ-ray LAT transients shown in **Figure 3.1** with relevant statistics and fitted parameters.
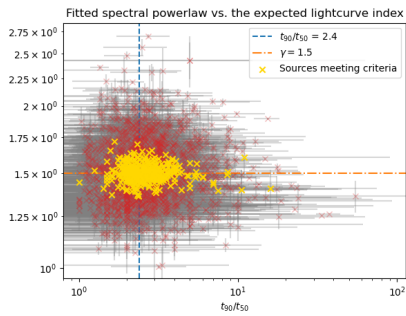
Figure 3.4: Visualization of selection cuts applied to the GBM sources. Cut on distance not shown because it imposes the weakest constraints.
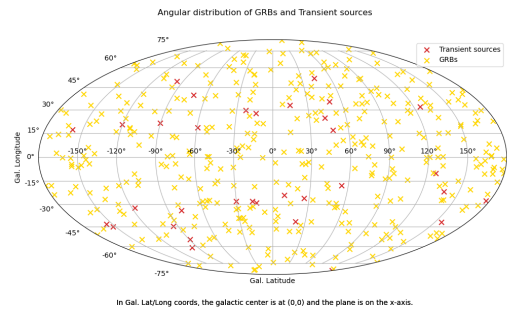
Figure 3.5: Angular distribution of PBH-candidate GRBs and Transient *gamma*-ray sources as catalogued in the GBM and Transient source catalogs.

3.2 Analysis of short-duration GRB sources

In the domain of GRB sources, we use the Fermi GBM Burst Catalog, which lists high-energy sources detected in 14 years of operation [2][21][4][39].

We first constrain by the spectral and lightcurve powerlaw index. For the GBM late-stage evaporation powerlaw index $\beta = -0.33$ we expect $t_{90}/t_{50} = 2.4$. Similarly, for energy pivots $\lesssim$ GeV and $t_{90} \lesssim 10^5$s, we expect for the spectral index to be $\gamma(\tau) = 1.5$. Lastly, we derive the expected distance with respect to the normalized photon flux and require it to be $\lesssim 2.7 \times 10^{-4}$pc following the maximal detection curve for the GBM. For the latter two constraints, we use the fitted values for spectral index and normalization provided by the catalog. These cuts are visualized in **Figure 3.4**, excepting the cut on distance which is relatively weak. There are 388 GRB candidate sources resulting from the above constraints.

As is shown in **Figure 3.5**, there is a wide angular distribution of sources

39

for both transient and GRB sources, as expected with the local isotropic distribution of dark matter. The ratio of sources in the northern to southern hemisphere is 1.04, whereas the ratio of sources in the western to eastern hemispheres is 0.879 – indicating a slightly larger abundance in the eastern hemisphere of the sky. Previous research into very-short GRBs using the BATSE monitor discovered similar overdensity in the eastern hemisphere, caused possibly by halo clumping [18]. Note also that isotropy is also an indication of extragalactic γ-ray sources, so this fact alone only rules out the anisotropic overdensity expected from galactic origin.

3.3 Associating transient and GRB sources

We model the association of GRBs with nearby transient sources as a function of the expected proper motion over time. We consider any bursts where the difference between the LAT and GRB localizations for right ascension (RA) and declination (DEC), with allowance to errors $\Delta\theta$, allowing for 1 degree of proper motion per year scaled by time (the initial detection time for the transient source and $t_0^{\text{trans.}}$ and the GRB burst time t^{grb}).

$$
\begin{aligned}
\sqrt{\left(\text{RA}^{\text{grb}} - \text{RA}^{\text{trans.}}\right)^2 + \left(\text{DEC}^{\text{grb}} - \text{DEC}^{\text{trans.}}\right)^2} - \left(\Delta\theta^{\text{grb}} + \Delta\theta^{\text{trans.}}\right) \\
\leq \frac{1\text{deg}}{\text{yr}} \times \left(t^{\text{grb}} - t_0^{\text{trans.}}\right)
\end{aligned}
\tag{3.1}
$$

Of the 35 transient sources, we found 14 which have at least one GRB detected within the above limit. In an ideal case the GRB follows the last (most recent) observation of a transient source and appears brighter than its transient counterpart as it corresponds

with the PBH explosion. We visualize this relationship with **Figure 3.6**, which shows the relationship between the transient flux and the corresponding flux of GRBs in the 1 degree-per-year localization. Relevant catalog information for these sources is shown in **Table 3.2**.

We find that for all the fitted transient sources, their corresponding GRBs lie too far outside the confidence interval to be reasonably associated for the standard PBH lightcurve. We can mention again some likelihood that a PBH lightcurve constrained by dark degrees of freedom could also produce such a pattern but, at current understanding for the values of τ_D and $\Delta\alpha/\alpha$, it is difficult to make this argument. We conclude that there is too little evidence to associate these GRBs with meaningful confidence.

3.4   Discussion of results

Beginning first with LAT transient sources, one must acknowledge that a good number of parameterizations fall within areas where there exists substantial proper motion. In this regard, there is a balancing act. First, that the fitted values for transient lifetime are subject to a substantial amount of bias from the model due to the small number of photons which constitute each available ($\sim$monthly binned) lightcurve. This ironically forces the second point, which is that spectral analysis of transient sources with a relatively small observation window (for example, $T_{\mathrm{obs}} \sim 1$ month at distances $\sim 10^{-3}$pc) may be a more effective method of detecting evaporating PBHs with long lifetimes. Further investigation for differentiating few-photon instantaneous energy spec-
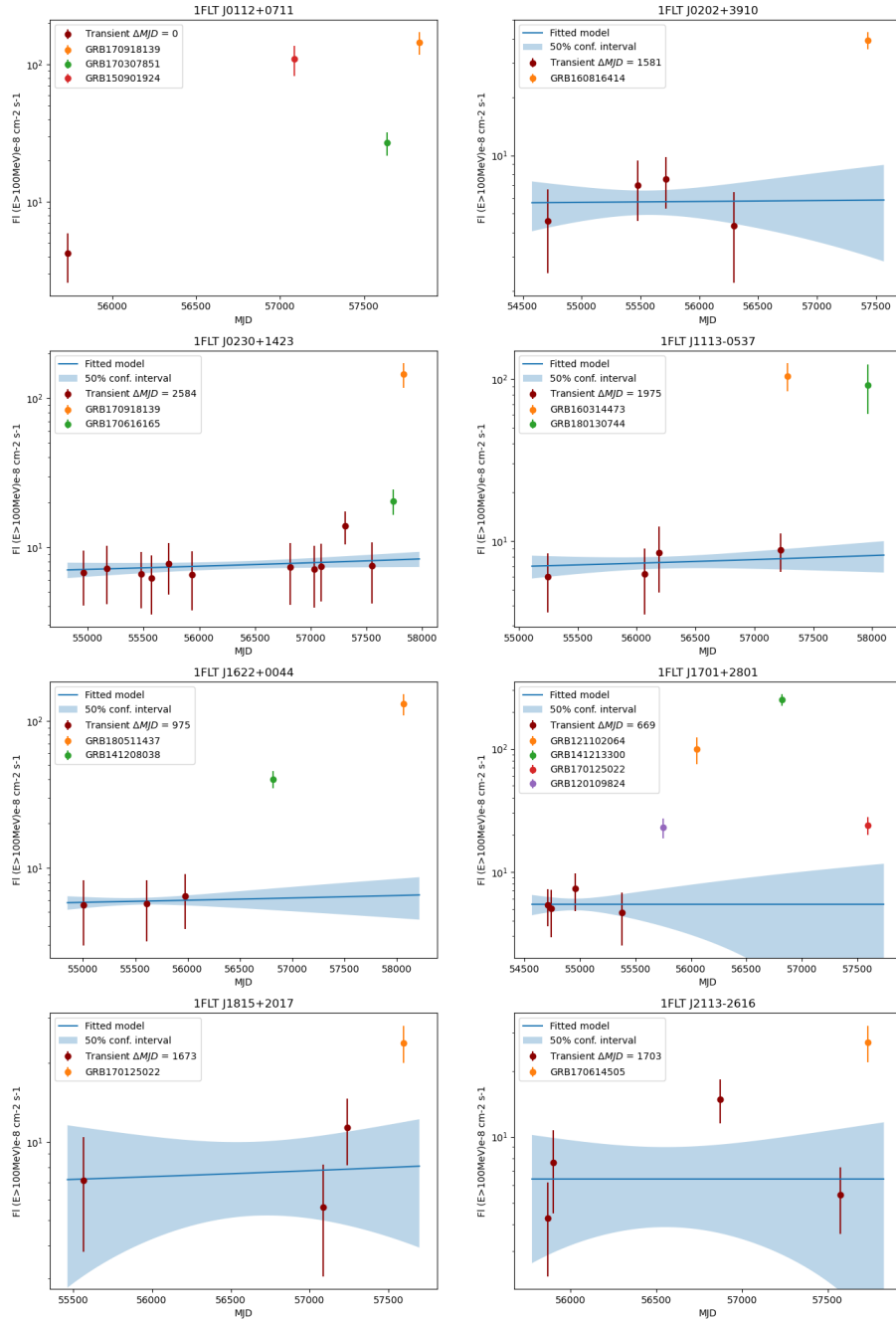
Figure 3.6: For each LAT transient source, we plot the flux of possibly associated GRBs. We find that, for our fitted powerlaw model, we cannot suggest any GRBs produced by the GBM which could be the end product of the longer-lived LAT transient source.

Source name	RA (deg)	DEC (deg)	Rad. Err. (deg)	Flux (erg/cm^2/s)	Flux err.	t_{90}/t_{50}	t_{90}/t_{50} err.
GRB170614505	310.99	-37.91	15.16	2.71e-07	5.19e-08	2.10	1.62
GRB160314473	161.99	2.83	19.99	1.04e-06	2.04e-07	8.67	15.87
GRB170918139	36.56	3.52	17.81	1.45e-06	2.67e-07	4.00	6.96
GRB180511437	257.78	9.07	10.16	1.30e-06	2.09e-07	2.58	1.78
GRB170307851	13.54	9.54	0.05	2.69e-07	5.10e-08	2.06	0.79
GRB141208038	239.16	10.97	9.49	4.01e-07	5.41e-08	1.93	0.57
GRB150901924	16.34	13.52	17.12	1.09e-06	2.73e-07	2.00	9.29
GRB121102064	258.47	14.09	12.15	9.90e-07	2.45e-07	1.60	1.52
GRB141213300	248.19	18.06	8.72	2.49e-06	2.72e-07	4.00	3.62
GRB170616165	49.51	19.67	12.12	2.04e-07	3.93e-08	2.27	0.74
GRB170125022	264.14	28.58	12.65	2.40e-07	3.93e-08	2.44	1.49
GRB120109824	251.33	30.80	11.33	2.29e-07	4.15e-08	2.25	0.72
GRB160816414	25.32	43.70	19.13	3.93e-07	3.94e-08	2.19	1.53
GRB180130744	136.83	52.69	68.08	9.20e-07	3.14e-07	2.00	7.58

Source name	MJD (days)	t_{90} (s)	t_{90} err.	γ	γ pos. err.	γ neg. err.
GRB170614505	5.77e+04	5.38	1.64	-1.45	0.12	0.12
GRB160314473	5.73e+04	1.66	0.73	-1.51	0.13	0.13
GRB170918139	5.78e+04	0.13	0.16	-1.45	0.08	0.08
GRB180511437	5.81e+04	1.98	0.97	-1.52	0.10	0.10
GRB170307851	5.76e+04	28.42	1.72	-1.57	0.10	0.10
GRB141208038	5.68e+04	14.34	1.45	-1.49	0.07	0.07
GRB150901924	5.71e+04	0.26	1.15	-1.40	0.17	0.17
GRB121102064	5.60e+04	2.05	1.38	-1.52	0.16	0.16
GRB141213300	5.68e+04	0.77	0.51	-1.54	0.05	0.05
GRB170616165	5.77e+04	56.32	6.08	-1.39	0.12	0.12
GRB170125022	5.76e+04	3.90	1.12	-1.45	0.10	0.10
GRB120109824	5.58e+04	38.66	3.11	-1.50	0.11	0.11
GRB160816414	5.74e+04	11.78	3.81	-1.54	0.06	0.06
GRB180130744	5.80e+04	0.26	0.92	-1.53	0.23	0.23

Table 3.2: The unassociated GRB sources pictured in **Figure 3.6** with relevant statistics. Note that MJD is Modified Julian Days.

trum from other γ-ray sources is required to appropriately judge this possibility.

We have a wider number of criteria in the GBM and a correspondingly large number of GRBs on which to apply them. We attempt to constrain sources further by investigating sources which follow LAT transients in the same ROI, but find no sources which are well-associated as modelled. Several sources still garner interest due to qualitative attributes, such as GRB141213300 shown in **Figure 3.7**. In particular, we can see a qualitatively clean peak with sharp rising and falling edges, indicative of our expected lightcurve shape. Additionally, the higher-energy BGO detector has a slightly higher countrate and leads the NaI detectors by $\sim$ 100ms. As discussed previously, future research could apply broadband spectral analysis (beyond simple comparison of spectral index) to better associate possible PBH evaporation transient and GRB signals.
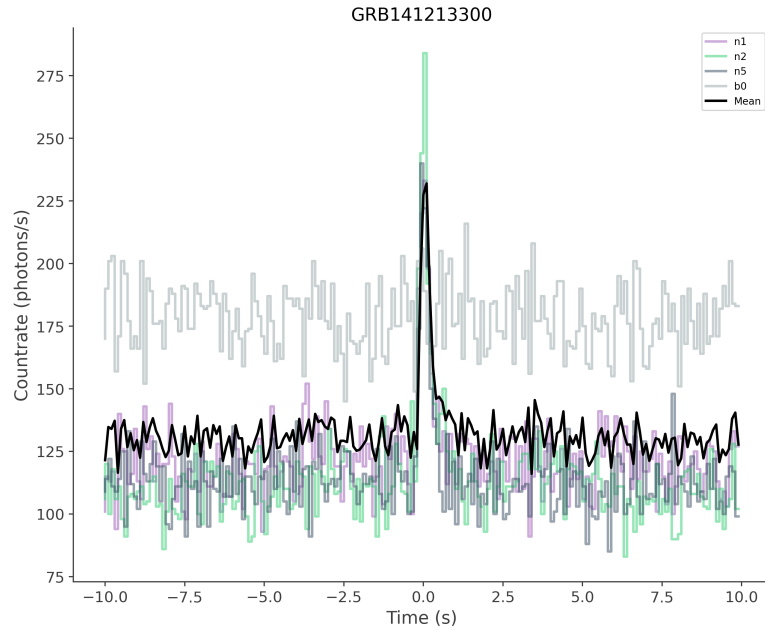
Figure 3.7: GRB141213300 satistifes all constraints, lying in the scaled ROI of 1FLT J1701+2801. The signal from its brightest four detectors, the NaI (colored n1, n2, n5) and BGO (grey b0) detectors, binned on 100ms and overlain with their average (black). This source typifies many of the ideal characteristics in a candidate PBH GRB, including sharp rising and falling edges, and a slight temporal lead in the BGO signal versus that of the NaI.

Chapter 4

Conclusions

The potential of directly observing a PBH explosion carries immense implications for our understanding of the universe, from cosmology to particle physics. While the existence of PBHs as a candidate for dark matter has been theorized for decades, direct detection of an evaporating PBH would provide invaluable insights into yet-undiscovered high-energy particles and dark radiation.

In the first chapter, we provide an introduction and overview into the state of the field for evaporating primordial black holes. We outline why they solve problems in dark matter and discuss the means by which they could have formed. We describe, in particular, the physics behind the evolution of photon emission in black holes.

In Chapter 2, we demonstrate the constraints on the detectability of PBHs, taking into account various telescopes and the effects of proper motion. While the limitations on PBH detection are significant at $\lesssim 10^{-2}$pc, we outline several characteristics that can be used to differentiate PBHs from other gamma-ray sources. These include

46

the time-evolved spectral index γ and the t_{90}/t_{50} ratio, which can serve as proxies for the parameterized powerlaw index β. Moreover, we discuss the effect of dark sector degrees of freedom on the photon lightcurve, which can further aid in identifying PBHs.

In Chapter 3, we apply the constraints we've developed to two areas of interest: close proximity, long duration γ-ray sources and short duration GRB sources. We investigate the *Fermi* mission's transient and γ-ray burst catalogs and find several candidates which match many of our constraints. We extrapolate fitted models of the transient sources to investigate if GRB sources in the same localization appear within the the appropriate bounds. While our analysis did not produce any conclusive evidence of such associations, it offers a framework for future studies and observations.

Overall, the potential for direct detection of a PBH explosion holds immense promise for advancing our understanding of the universe. As observational and analysis capabilities continue to improve, further investigation and refinements of the constraints presented in this report will undoubtedly lead to new insights in the physics of evaporating black holes.

Bibliography

[1] HAWC Collaboration A. Albert et. al. Constraining the local burst rate density of primordial black holes with HAWC. *Journal of Cosmology and Astroparticle Physics*, 2020(04):026–026, apr 2020.

[2] Fermi Collaboration A. von Kienlin et. al. The fourth fermi-gbm gamma-ray burst catalog: A decade of data. *The Astrophysical Journal*, 893(1):46, apr 2020.

[3] Fermi Collaboration A. von Kienlin et. al. The fourth fermi-GBM gamma-ray burst catalog: A decade of data. *The Astrophysical Journal*, 893(1):46, apr 2020.

[4] Fermi Collaboration Andreas von Kienlin et. al. The second fermi gbm gamma-ray burst catalog: The first four years. *The Astrophysical Journal Supplement Series*, 211(1):13, feb 2014.

[5] Alexandre Arbey and Jérémy Auffinger. BlackHawk: a public code for calculating the hawking evaporation spectra of any black hole distribution. *The European Physical Journal C*, 79(8), aug 2019.

[6] Alexandre Arbey and Jérémy Auffinger. Physics beyond the standard model with BlackHawk v2.0. *The European Physical Journal C*, 81(10), oct 2021.

[7] Christian W. Bauer, Nicholas L. Rodd, and Bryan R. Webber. Dark matter spectra from the electroweak to the Planck scale. *JHEP*, 06:121, 2021.

[8] J. Binney and S. Tremaine. *Galactic Dynamics*. Princeton series in astrophysics. Princeton University Press, 1987.

[9] Johannes Buchner. A statistical test for Nested Sampling algorithms. *Statistics and Computing*, 26(1-2):383–392, January 2016.

[10] Johannes Buchner. Collaborative Nested Sampling: Big Data versus Complex Physical Models. , 131(1004):108005, October 2019.

[11] Johannes Buchner. UltraNest - a robust, general purpose Bayesian inference engine. *The Journal of Open Source Software*, 6(60):3001, April 2021.

[12] HAWC Collaboration Cao, Zhen et. al. The large high altitude air shower observatory (lhaaso) science book (2021 edition). 2019.

[13] B. J. Carr and S. W. Hawking. Black holes in the early Universe. *Monthly Notices of the Royal Astronomical Society*, 168:399–416, August 1974.

[14] B. J. Carr, Kazunori Kohri, Yuuiti Sendouda, and Jun'ichi Yokoyama. New cosmological constraints on primordial black holes. *Physical Review D*, 81(10), may 2010.

[15] Bernard Carr and Florian Kühnel. Primordial black holes as dark matter: Recent developments. *Annual Review of Nuclear and Particle Science*, 70(1):355–394, oct 2020.

[16] Bernard Carr, Martti Raidal, Tommi Tenkanen, Ville Vaskonen, and Hardi Veermäe. Primordial black hole constraints for extended mass functions. *Physical Review D*, 96(2), jul 2017.

[17] Fermi Collaboration Charles Meegan et. al. THE FERMI GAMMA RAY BURST MONITOR. *The Astrophysical Journal*, 702(1):791–804, aug 2009.

[18] D.B Cline, C Matthey, and S Otwinowski. Evidence for a galactic origin of very short gamma ray bursts and primordial black hole sources. *Astroparticle Physics*, 18(5):531–538, feb 2003.

[19] Douglas Clowe, Maruš a Bradač, Anthony H. Gonzalez, Maxim Markevitch, Scott W. Randall, Christine Jones, and Dennis Zaritsky. A direct empirical proof of the existence of dark matter. *The Astrophysical Journal*, 648(2):L109–L113, aug 2006.

[20] Fermi Collaboration. Fermi lat low-energy events catalog.

[21] Fermi Collaboration David Gruber et. al. The fermi gbm gamma-ray burst spectral catalog: Four years of data. *The Astrophysical Journal Supplement Series*, 211(1):12, feb 2014.

[22] T.C Weekes et. al. VERITAS: the very energetic radiation imaging telescope array system. *Astroparticle Physics*, 17(2):221–243, may 2002.

[23] Torbjörn Sjöstrand et. al. An introduction to PYTHIA 8.2. *Computer Physics Communications*, 191:159–177, jun 2015.

[24] Jordan Goodman and John Pretz. Sensitivity and Status of the HAWC. In *International Cosmic Ray Conference*, volume 33 of *International Cosmic Ray Conference*, page 3016, January 2013.

[25] Zas E. MacGibbon J. H. Weekes T. C. Halzen, F. Gamma rays and energetic particles from primordial black holes. *Nature*, 08 1991.

[26] S. Hawking. Black hole explosions? *Nature*, 1974.

[27] Dan Hooper, Alexander V. Belikov, Tesla E. Jeltema, Tim Linden, Stefano Profumo, and Tracy R. Slatyer. The isotropic radio background and annihilating dark matter. *Phys. Rev. D*, 86:103003, Nov 2012.

[28] Kiyoharu Kawana and Ke-Pan Xie. Primordial black holes from a cosmic phase transition: The collapse of fermi-balls. *Physics Letters B*, 824:136791, jan 2022.

[29] H. Krawczynski, D.A. Carter-Lewis, C. Duke, J. Holder, G. Maier, S. Le Bohec, and G. Sembroski. Gamma–hadron separation methods for the VERITAS array of four imaging atmospheric cherenkov telescopes. *Astroparticle Physics*, 25(6):380–390, jul 2006.

[30] F. Kunzweiler, B. Biltzinger, J. Greiner, and J. M. Burgess. Automatic detection of long-duration transients in ifermi/i-GBM data. *Astronomy &amp Astrophysics*, 665:A112, sep 2022.

[31] Fermi-LAT Collaboration L. Baldini et. al. Catalog of long-term transient sources in the first 10 yr of fermi-lat data. *The Astrophysical Journal Supplement Series*, 256(1):13, sep 2021.

[32] journal = The Astrophysical Journal LAT Collaboration. Search for gamma-ray emission from local primordial black holes with the fermi large area telescope, 2018.

[33] et. al. M. Ackermann. The spectrum of isotropic diffuse gamma-ray emission between 100 mev and 820 gev. *The Astrophysical Journal*, 799(1):86, jan 2015.

[34] Fermi Collaboration M. Ajello et. al. A decade of gamma-ray bursts observed by ifermi/i-LAT: The second GRB catalog. *The Astrophysical Journal*, 878(1):52, jun 2019.

[35] Jane H. MacGibbon and B. R. Webber. Quark- and gluon-jet emission from primordial black holes: The instantaneous spectra. *Phys. Rev. D*, 41:3052–3079, May 1990.

[36] Stacy S. McGaugh. The surface density profile of the galactic disk from the terminal velocity curve. *The Astrophysical Journal*, 816(1):42, dec 2015.

[37] Gamma-Ray Astrophysics Team Michael S. Briggs. Fermi gbm, 2018.

[38] A. Neronov and D. Semikoz. Possibility of measurement of cosmic ray electron spectrum up to 100 tev with two-layer water cherenkov detector array, 2021.

[39] Fermi Collaboration P. Narayana Bhat et. al. The third fermi gbm gamma-ray burst catalog: The first six years. *The Astrophysical Journal Supplement Series*, 223(2):28, apr 2016.

[40] Wilkinson Microwave Anisotropy Probe. Nine year microwave sky, 2014.

[41] S. Profumo. *An Introduction to Particle Dark Matter*. Advanced textbooks in physics. World Scientific Publishing Europe Ltd., 2017.

[42] HAWC Collaboration R. Alfaro et. al. Gamma/hadron separation with the HAWC observatory. *Nuclear Instruments and Methods in Physics Research Section A: Accelerators, Spectrometers, Detectors and Associated Equipment*, 1039:166984, sep 2022.

[43] Gamma-Ray Astrophysics Team Robert S. Mallozzi. The batse experiment, 2018.

[44] Vera C. Rubin and Jr. Ford, W. Kent. Rotation of the Andromeda Nebula from a Spectroscopic Survey of Emission Regions. , 159:379, February 1970.

[45] Regina Caputo Riccardo Rando Eric Charles Seth Digel Simone Maldera, Matthew Wood and Luca Baldini. Fermi lat performance, 2021.

[46] G. SINNIS, A. SMITH, and J. E. MCENERY. HAWC: A NEXT GENERATION ALL-SKY VHE GAMMA-RAY TELESCOPE. *The Tenth Marcel Grossman Meeting*, feb 2006.

[47] Torbjörn Sjöstrand, Stephen Mrenna, and Peter Skands. PYTHIA 6.4 physics and manual. *Journal of High Energy Physics*, 2006(05):026–026, may 2006.

[48] Fermi Collaboration Tashiro et. al. Status of grb observations with the suzaku wideband all-sky monitor. 1000, 02 2008.

[49] Tramacere, A., Sliusar, V., Walter, R., Jurysek, J., and Balbo, M. Radio- response in blazars as a signature of adiabatic blob expansion. *A&A*, 658:A173, 2022.

[50] David Tsang, Jocelyn S. Read, Tanja Hinderer, Anthony L. Piro, and Ruxandra Bondarescu. Resonant shattering of neutron star crusts. *Physical Review Letters*, 108(1), jan 2012.

[51] T.N. Ukwatta, D.R. Stump, J.T. Linnemann, J.H. MacGibbon, S.S. Marinelli, T. Yapici, and K. Tollefson. Primordial black holes: Observational characteristics of the final evaporation. *Astroparticle Physics*, 80:90–114, jul 2016.

[52] Giacomo Vianello, Robert J. Lauer, Patrick Younk, Luigi Tibaldo, James M. Burgess, Hugo Ayala, Patrick Harding, Michelle Hui, Nicola Omodei, and Hao Zhou. The multi-mission maximum likelihood framework (3ml), 2015.

[53] Risa H. Wechsler and Jeremy L. Tinker. The connection between galaxies and their dark matter halos. *Annual Review of Astronomy and Astrophysics*, 56(1):435–487, sep 2018.